Supporting information

Light Cycling as a Key to Understanding the Outdoor Behaviour of Perovskite Solar Cells

Mark Khenkin[1*], Hans Köbler[1*], Marko Remec[1,2], Rajarshi Roy[1$], Ulas Erdil[1], Jinzhao Li[1], Nga Phung[1#], Ghefar Adwan[1], Gopinath Paramasivam[1], Quiterie Emery[1], Eva Unger[1], Rutger Schlatmann[1], Carolin Ulbrich[1§], Antonio Abate[1§]

[1] Helmholtz-Zentrum Berlin für Materialien und Energie, Helmholtz-Zentrum-Berlin, 12489 Berlin, Germany

[2] Laboratory of Photovoltaics and Optoelectronics, University of Ljubljana, Faculty of Electrical Engineering, Trzaska cesta 25, SI-1000 Ljubljana, Slovenia

* Authors contributed equally to this work.

$ Present address: Institut für Photovoltaik, Universität Stuttgart, Pfaffenwaldring 47, 70569 Stuttgart, Germany

Present address: Department of Applied Physics, Eindhoven University of Technology, 5600 MB Eindhoven, The Netherlands.

§ Corresponding authors. Antonio.abate@helmholtz-berlin.de Carolin.ulbrich@helmholtz-berlin.de

Supplementary Note 1. Device fabrication

Four types of PSCs were investigated in this study. All have p-i-n configuration with the layer sequences shown in Table S1.

Table S1. Device stack of the four types of PSCs used in the study.

Name	**Structure**						
1cat_SAM	ITO	MeO-2PACz (SAM)	$FAPbI_3$	LiF	C_{60}	SnO_2	Cu
2cat_SAM	ITO	2PACz (SAM)	$Cs_{0.15}FA_{0.85}PbI_{2.55}Br_{0.45}$		C_{60}	SnO_2	Cu
3cat_SAM	ITO	MeO-2PACz (SAM)	$Cs_5(MA_{15}FA_{85})_{95}Pb(I_{85}Br_{15})_3$		C_{60}	SnO_2	Cu
3cat_NiO	ITO	NiO	$Cs_5(MA_{15}FA_{85})_{95}Pb(I_{85}Br_{15})_3$		C_{60}	SnO_2	Cu

To fabricate devices, firstly pre-structured ITO glass substrates (*Automatic Research*, 25 x 25 mm, resistivity 15 Ω /sq), were cleaned properly with a 2% Mucasol water solution followed by an ultrasonic (US) bath cleaning with DI water, acetone and isopropanol. Each step was performed for 15 min in an US bath at 40 °C. Afterwards, the substrates were treated with UV-Ozone for 15 min.

The preparation of the self-assembled monolayers (SAMs) MeO-2PACz and 2PACz was performed by the instructions given in previously published literature[1]. In brief, 100 µl of a 1 mmol/l solution were dropped in the middle of the substrate and given 5 s of rest before starting the spin coating. The spin coating was then performed at 3000 rpm for 30 s followed by annealing for 10 min at 100 °C. [1]

Nickel oxide was deposited from a 0.15 M of $NiCl_2{\cdot}6H_2O$ solution in anhydrous 2-Methoxyethanol with the addition of 20 µl of 65% HNO_3.[2] The solution was heated overnight at 60 °C under continuous shaking. Before spin coating, 85 µl of the solution were deposited in the centre of the substrate. The spin coating was performed at 500 rpm for 1 s and 4000 rpm for 30 s. The substrates were immediately annealed at 75 °C for 10 min followed by annealing at 120 °C for 15min and 300 °C for 1 hour.[2]

$FAPbI_3$ films in 1cat_SAM solar cells were prepared via slot-die coating following the procedure described in [3]. 10 mol% Methylammonium chloride (MACl) was used as additive to stabilize α-FAPbI3 phase. The slot-die coated thin films were annealed at 150 °C for 15 mins.

For the deposition of the perovskite $Cs_{0.15}FA_{0.85}PbI_{2.55}Br_{0.45}$, for 2cat_SAM cells, a precursor solution of 1.3 M concentration was prepared by dissolving PbI_2 (901.9 mg), $PbBr_2$ (243.3 mg), FAI (371.1 mg), and CsI (114.8 mg) powders in DMF/DMSO (1600:400 µl) in a single vial. The solution was kept in a shaker at 60 °C until it appeared transparent. Subsequently, the perovskite solution was spin-coated on top of the 2PACz layers at the speed of 3500 rpm for 40 s including a 5 s acceleration at the start of program. 250 µl anisole was dropped on the wet perovskite 10 s before the end of the program. The perovskite films were then annealed at 100 °C for 30 min.

The perovskite solution for the $Cs_5(MA_{15}FA_{85})_{95}Pb(I_{85}Br_{15})_3$ perovskite ("3cat", a slight variation of the original "triple cation" perovskite [4]) was prepared following a previously reported procedure.[5] First, $PbBr_2$ and PbI_2 solutions with a nominal concentration of 1.5 M were prepared by addition of a 4:1 mixture of DMF:DMSO and were continuously shaken at 60 °C overnight. These stock solutions were added to the MABr and FAI powders to obtain a 1.24 M solution. The $FAPbI_3$ and $MAPbBr_3$ solutions were then mixed in at 5.7:1(v:v) volume ratio. In the final stage, a 1.5 M solution of CsI in DMSO was added to the final perovskite solution with a 5:95 (v:v) volume ratio to obtain the desired $Cs_5(MA_{15}\ FA_{85})_{95}Pb(I_{85}Br_{15})_3$ perovskite solution. Before spin coating, 100 µl of the perovskite solution was released on the SAM and NiO-covered substrates. On NiO substrates, the solution was spread with the pipette tip for better surface coverage. The spin coating was performed with 5 s of acceleration to 4000 rpm followed by 35 s steady rotation at 3500 rpm. Anisole was used as an antisolvent and dropped 6 s before the end of the spinning program. The substrates were annealed at 100 °C for 30 min. The procedure resulted in layers of approximately 400-500 nm thickness.

Films of C_{60} of were deposited via thermal evaporation at app. 360 °C. By monitoring the deposition rate, a thickness of 23 nm was achieved. The ETL stack was completed by atomic layer deposition (ALD) of a 20 nm SnO_2 layer at 80 °C.

Devices were completed by a thermal evaporation of 100 nm layer of copper as the counter electrode. A mask was used during the evaporation to give the solar cells an active area of 0.16 or 1 cm^2. All steps except the substrate cleaning were carried out in nitrogen atmosphere.

Device encapsulation

Two different device encapsulation procedures, referred to as the "glass-glue-glass" and the "three glass" encapsulations were performed in this work. The two geometries are shown schematically in Figure S1.

a) The "glass-glue-glass" encapsulation is a simple procedure that consists in gluing on the device a cavity glass slightly smaller than the glass substrate with an adhesive (Blufixx for metal, glass and stone) applied on the edges of the cavity glass. The adhesive is cured by UV-lamp curing for approximately 30 seconds. Therefore, the contacts of the cells remain accessible, and the active areas are protected from the external environment.
a) The "three glass" encapsulation was described in a previous publication where it was referred to as the "COM" encapsulation [6]. In short, it consists in sandwiching the device on its substrate between two encapsulation glasses with polyolefin elastomer (Mitsui, Solar ASCE TR02BA-50T) as an encapsulant and butyl rubber (Quanex SET LP03, 3948) as an edge sealant. The package is processed inside a vacuum laminator for 20 minutes at 150°C and the contacts are accessed through tinned copper solar ribbons glued on the cathodes and the anodes of the devices.

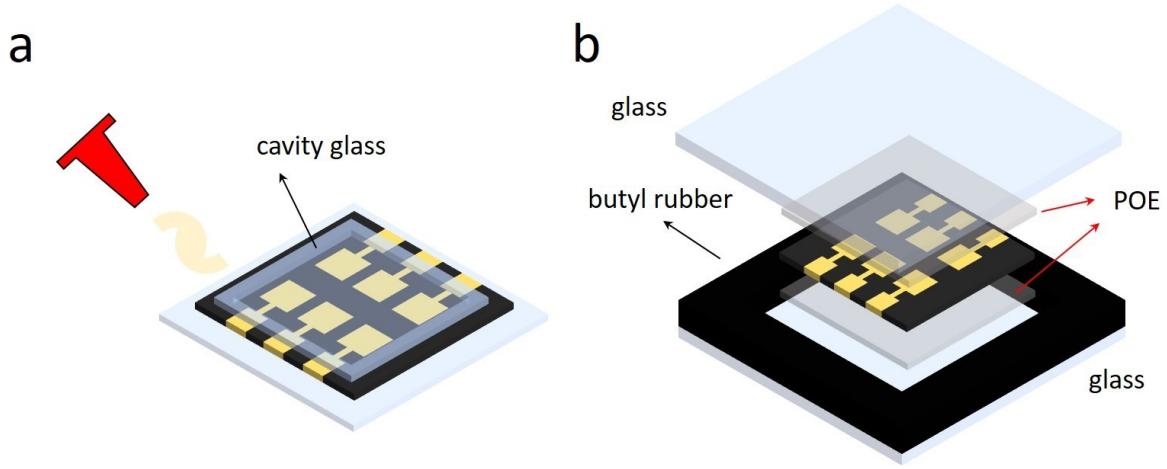

Figure S1 Schematic of the "glass-glue-glass" (a) and "three glass" (b) encapsulation methods used in this work for outdoor tests.

Supplementary Note 2. Indoor and outdoor aging tests

Table S1 summarizes the aging conditions used in this study and classifies them according to ISOS protocols [7]. According to the Perovskite database project (contains data until June 2021) [8], the vast majority of published studies conducted on PSCs stability are performed using constant levels of stress factors (mostly ISOS-D and ISOS-L, see Figure S2) often with a short duration. Although new relevant research has been published since June 2021, Figure S1 still characterizes the general trend. In this work, we show that cycling the stress factors, particularly light, is essential to mimic the results of aging in outdoor conditions.

Table S1 : Conditions of the performed ageing tests.

	Test 1 "Constant indoor"	**Test 2 "Cycled indoor"**	**Test 3 "Outdoor"**
light source	simulated light, 100 mW/cm^2	simulated light, 100 mW/cm^2	natural sunlight
illumination	constant	cycled (12 h/12 h)	varying
temperature	25 °C active-controlled	25 °C active-controlled	varying
electronic load	MPP tracking	MPP tracking	MPP tracking
test atmosphere	N_2 flow	N_2 flow	ambient air
encapsulation	none or lamination	none	"glass-glue-glass" or "three glass" lamination
ISOS protocol	**ISOS-L1I**	**ISOS-LC-1I**	**ISOS-O-2**

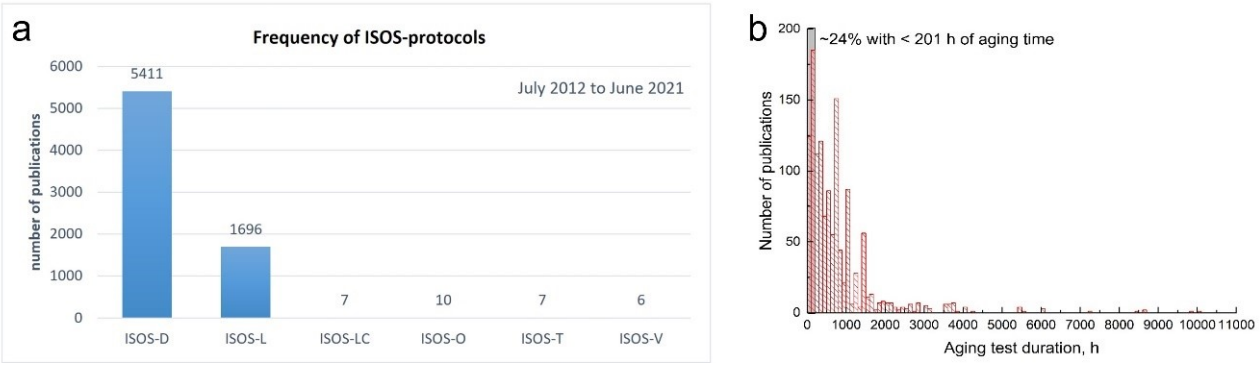

Figure S2 (a) Number of publications with PSCs using different classes of ISOS-protocols. (b) The aging time duration for the reported photo-stability tests (ISOS-L). Data obtained from the Perovskite Database [8]. Publications between July 2012 and June 2021 are included.

Indoor Constant Illumination

Solar cells were aged in a custom-built High-throughput Ageing Setup[9]. To MPP track all cells individually, special electronics were used and a perturb and observe algorithm[10] was applied with a delay time of 1 s and a voltage step-width of 0.01 V. PCE_{MPP} values were recorded every 2 min for each cell automatically. The devices were kept at 25 °C at all time with actively controlled Peltier-elements and with active areas touching a heatpad for direct thermal coupling. Aging was performed under a continuous flow of nitrogen in an otherwise sealed box with no additional encapsulation used, except for the control experiment shown in Supplementary Note 10. Light with 100 mW/cm^2 intensity (1 sun) was provided by a class C metal-halide lamp using a H6 filter. Figure S3 shows the spectrum of the light source in comparison to AM1.5G. The light intensity was actively controlled with the help of a silicon irradiation-sensor which was calibrated using a KG3 silicon reference cell from Fraunhofer ISE. The test is in accordance with the protocol ISOS-L-1I.[7]

The slight oscillations on the continuous light with the period of 24 h is due to the simultaneous execution of both cycled and constant light experiments in the same setup which results in a minor difference in light intensity when the shutters are closed.

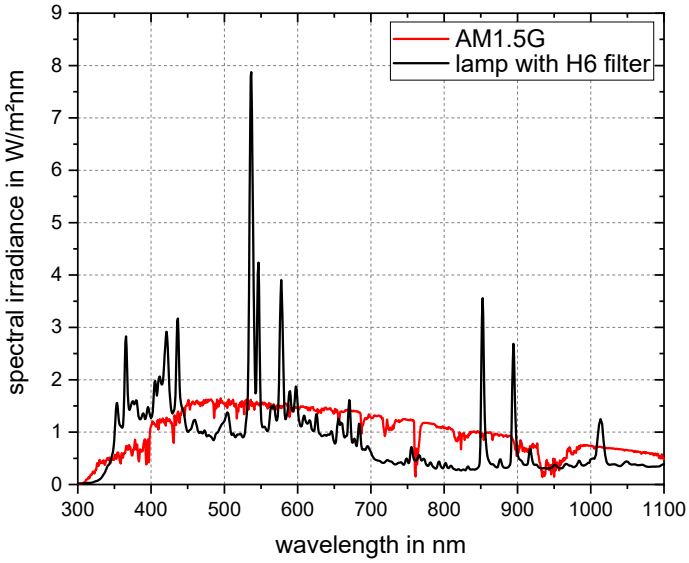

Figure S3 Spectrum of the lamp used for ageing solar cells indoors.

Indoor Cycled Illumination

Ageing tests with cycled illumination were carried out in the same way as the continuous light experiments described above, however an automated shutter was employed to switch between the light and dark condition with the period of 12 h each. Cells were disconnected while in the dark and under MPPT while under illumination. The JV curves are recorded twice per cycle (in forward and reverse direction). The test is in accordance with ISOS-LC-1I [7].

Outdoor Testing

Figure S4 Outdoor test field in Berlin (Germany) comprising of the fixed tilted rack for solar cells, meteo station, MPP tracking equipment, spectrometers for measurements of the sun spectrum and additional irradiance sensors in the plane of array and temperature sensors on the rear of the cells. The photograph on the right shows research size PSCs with area of ≤1 cm² which are investigated in this paper.

Outdoor measurements were carried out at the rooftop test field in Berlin, Germany (with coordinates 52°25'53.5 "N, 13°31'27.7 "E) in the period of May 2020-July 2022. Figure S4 shows photographs of the setup. The encapsulated samples were fixed on a 35°-tilted stand facing South. The irradiance measurements performed by *EKO ML-02* Si-pyranometer were recorded every 2 seconds using the *Picotech PT-104* datalogger. Cell temperature was measured with *DS18B20* temperature sensors attached to the rear of the encapsulated cells. The temperature of the cell inside the encapsulation is only marginally higher (2-8 °C depending on weather conditions) even at full sunlight illumination.
The power output was recorded by *MP2005M6* MPP trackers (LPVO), which kept cells at their MPP using the perturb and observe algorithm similar to the indoor system described above. The sun spectrum was recorded with a *WISER I* spectroradiometer by *EKO Instruments B.V.* From the measured sun spectra, the average photon energy (*APE*) was calculated using equation S1.

$$APE = \frac{\int_{350}^{1050} E_G(\lambda)d\lambda}{q\int_{350}^{1050} \Phi_G(\lambda)d\lambda}, \qquad \text{Equation S1}$$

where E_G is the measured global spectrum, Φ_G is the photon flux density, and q is the electron charge ($1.6e^{-19}$ J/eV). For a device-specific impact of the solar spectrum, we calculated the Spectral Factor *SF* using equation S2

$$SF = \frac{\int_{350}^{1050} SR(\lambda)E_G(\lambda)d\lambda \int_{350}^{1050} E_{ref}(\lambda)d\lambda}{\int_{350}^{1050} SR(\lambda)E_{ref}(\lambda)d\lambda \int_{350}^{1050} E_G(\lambda)d\lambda}, \quad \text{Equation S2}$$

where E_{ref} is the reference spectrum (AM1.5 G) and SR is the spectral response of the cell under study.

The dose of received irradiation in indoor experiments is not directly comparable to the dose in outdoor exposure, especially for constant illumination. The cumulative irradiance outdoors additionally strongly depends on the season and location. Figure S5 shows the irradiance in Berlin in 2020 recorded on our test field. The annual irradiance was ~1100 kWh with 40% of that accounting for the three summer months.

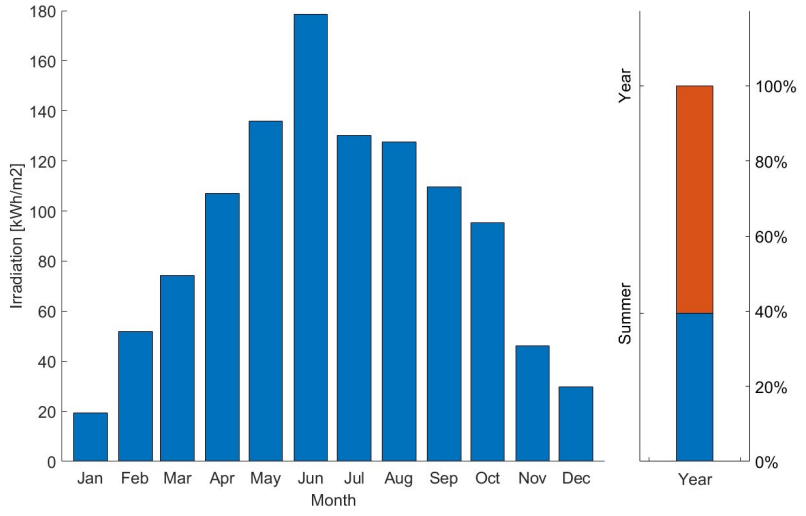

Figure S5 Monthly cumulative irradiance recorded on the outdoor test field in Berlin. The annual irradiance was ~1100 kWh, with ~40% of it during the 3 summer months.

As a reference device, a small area silicon-heterojunction solar cell (manufactured as descried in [11]) was installed outdoors and connected to the same tracking equipment.

Supplementary Note 3. Impact of sun irradiance and spectrum on PSCs' instantaneous power output

Figure S6 shows an example of MPP output from triple cation PSCs (3cat_SAM and 3cat_NiO) during one day of outdoor testing together with measured irradiance and temperature during that day. As with other PV technologies, PSCs' power output depends on irradiance, temperature, solar light spectrum and incidence angle. If each parameter's impact is known, one can reconstruct the expected cell behaviour under measured weather conditions. Comparison of such prediction with the de facto measured power can be used to track the device degradation [12]. As can be seen from Figure S6, the power output of the solar cells is following the irradiance mostly due to the linear dependence between irradiance and MPP current density (J_{MPP}), see Figure S7. Since outdoor data is much more likely to have outliers than indoor data, filtering the data is a standard practice. The outliers in Figure S7 were filtered by splitting the data into 10 W/m2 bins and discarding the data outside of 30-70% range around the median value both for V_{MPP} and J_{MPP}. Some deviations from this linearity are due to the changes in the incident sunlight spectrum and uncontrollable smaller influences such as soiling. This behaviour can also be seen in Figure S6 (middle row) that shows that the J_{MPP}-to-irradiance ratio during a day remains mostly constant. It deviates from being constant when the incident spectrum changes and resembles the average photon energy (APE) of the incident solar spectrum. APE is a common technology-agnostic figure of merit of the spectrum and was calculated using Equation S1 [13,14]. In essence, a blueshift in the incident spectrum leads to a marginally improved device current, while a redshift leads to a marginal decrease. The response of PSCs' current to APE changes is opposite to that of silicon solar cells due to the difference in bandgaps.

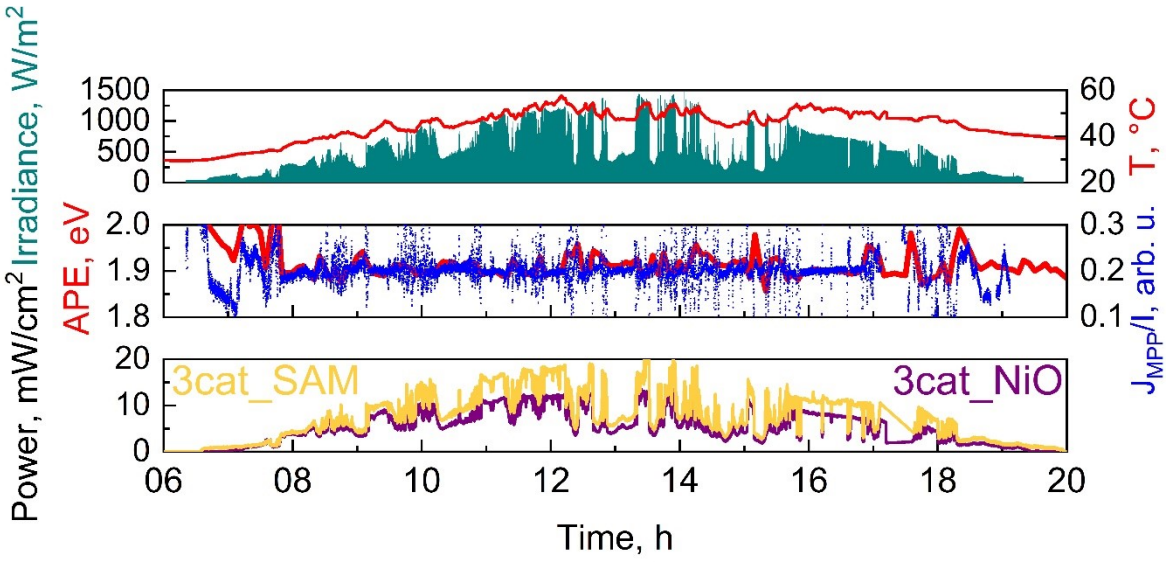

Figure S6 Impact of real-world weather changes on the PSC's power output: One day of outdoor exposure of 3cat_SAM and 3cat_NiO PSCs. The respective power output (c) measured via MPP tracking closely follows the measured irradiance and cell temperature (a). The average photon energy APE (red line in (b)), is calculated from spectral data measured in the plane of samples and plotted next to the ratio of Jmpp to irradiance (black dots in (b)) to highlight the effect of the sun spectrum.

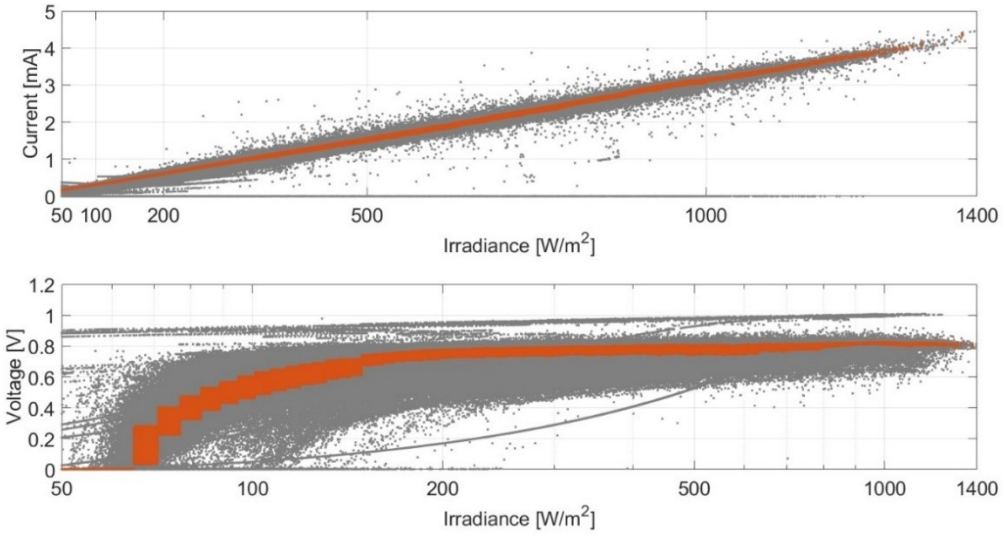

Figure S7 The correlation between current and voltage at MPP and irradiance for 1cat_SAM devices. The former is mostly linear, the later – logarithmic at irradiances above ~200 W/m². 11 months of data were used for this graph. The points in grey are filtered out, based on statistical analysis described above.

The changes in the sun spectrum during a day are not only due to the sun's position, but are also affected by presence of clouds, humidity, air pollution etc. On the longer timescale, seasonal variations in the solar spectrum become apparent. This will increase or decrease the PV performance depending mostly on the test field's location and the bandgap of the solar cell. Using the cell's spectral response (SR) or EQE, the spectral factor (*SF*) can be calculated (see Equation S2). It shows the relative changes in photocurrent under the real spectrum in comparison to the theoretically reached one under the AM1.5G standard spectrum (see Figure S8). A strong correlation between measured J_{MPP} divided by irradiance and the spectral factor is observed, confirming the suitability of this metric for power forecasting for PSCs. There is a noticeable increase of up to 10% in spectral gain in the summer period (in Berlin) for the studied PSCs. This effect contributes to the overall increase in performance ratio in summer but can only explain a fraction of this increase.

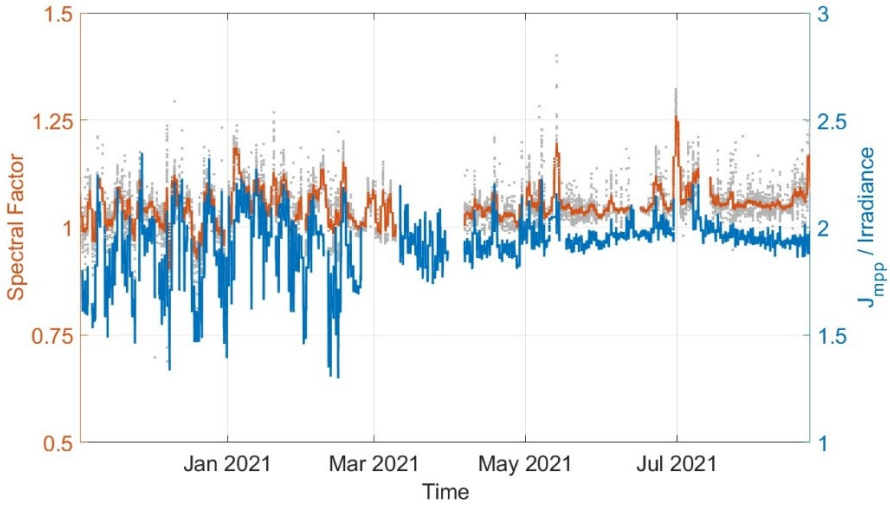

Figure S8 The correlation between 1cat_SAM devices' J_{MPP}-to-irradiance ratio (orange dots) and the spectral factor (blue line) over 10 months outdoor. In grey are points recorded at low irradiance (below 100 W/m²).

Supplementary Note 4. "Indoor" and "outdoor" temperature coefficient

The energy yield of solar cells decreases with increasing cell temperature. The magnitude of this effect is characterised by the temperature coefficient (TC), which can be calculated using Equation S3. PSCs are reported to have lower TCs compared to conventional PV based on silicon, mostly due to higher bandgap.

$$\gamma = \frac{\left(\frac{dPCE}{dT}\right)}{PCE_{25\,°C}}$$

Equation S3

Solar cells experience many combinations of external influences when exposed in the field. Outdoor data can thus be used to quantify the impact of weather on the devices' performance, such as low irradiance behaviour or temperature coefficients. However, we advise caution since the extraction of parameters from outdoor data might lead to a misinterpretation in case of PSCs. For example, E. Velilla et al. find temperature coefficients insignificant [15], while Stoichkov et al. even observed them being positive in some cases when derived from outdoor data [16], meaning that device efficiency improves with temperature. While a positive temperature coefficient may correlate to annealing effects or ion redistribution, it might also be entirely misleading due to unaccounted transient behaviour (see Figure S13 below) overlapping with temperature effects in the real-world conditions. When measured indoors, T coefficients of PSCs are negative like in all other PV technologies, lying in the range of approximately -0.1 to -0.3 %/K [12,17]. An exception poses devices with Spiro-OMeTAD, which show a non-linear dependence due to a peculiarity of this hole transporting material [18,19].

In Figure S9 we compare the temperature coefficients at different light intensities derived from indoor and outdoor measurements on 3cat_SAM and 3cat_NiO devices. To determine the temperature coefficient indoors, a device was placed onto a hotplate under a solar simulator (*Wavelabs Sinus-70,* AM1.5G with A+++ spectral accuracy). For temperature control during the experiment, a dummy cell connected to a temperature sensor was placed in an identical sample holder under the light source at the same time. The sample temperature was varied, and measurements were taken at 5 °C to 65 °C with steps of 10 °C. At each temperature, JV-scans were taken under different light intensities of 10, 20, 40, 60, 80 and 100 mW/cm^2. Before performing a JV scan in a new condition, the device was hold in the new condition for 5 min in order to equilibrate temperature and saturate light-soaking effects. After performing all measurements, the devices' efficiency was again tested in STC in order to exclude degradation effects from the measurements themselves. The temperature coefficients were then calculated according to Equation S3. A total of 5 cells for each HTL (hole transporting layer) were considered for the calculation.

Then temperature coefficients were also calculated using outdoor data for similar devices (Figure S9). We only used the data from the first four days of outdoor operation (Figure 2 in the main text) before degradation becomes noticeable. The data was filtered for each irradiance (at every point we took the irradiance interval of ±10 W/m^2). Then the coefficients were calculated using Equation S3. We also used the same procedure for the long-term outdoor data for 1cat_SAM devices as shown in Figure S10.

As shown in Figure S9, 3cat_SAM and 3cat_NiO PSCs show T-coefficients from appr. -0.1 to -0.3 %/K when measured in a controlled indoor environment after saturating the light-soaking effect, which is in the expected range. However, we observe significantly different values from outdoor data on the same type of devices, including some positive coefficients. Positive correlation in outdoor power with temperature was also reported to GaAs solar cells and explained by temperature-correlated spectral changes [20], which we believe cannot explain results reported here. Instead, we believe that the discrepancy shown in Figure S9 arises due to the presence of reversible processes that affect the PSC's daily behaviour and hence prohibit straightforward data interpretation as will be explained below. Importantly, this effect persists (or even becomes much clearer) when instead of the short outdoor time series over a few days data from several months is used for the calculation, which also includes seasonal weather variations (Figure S10). These examples showcase that caution must be taken when extracting PSC parameters from outdoor data.

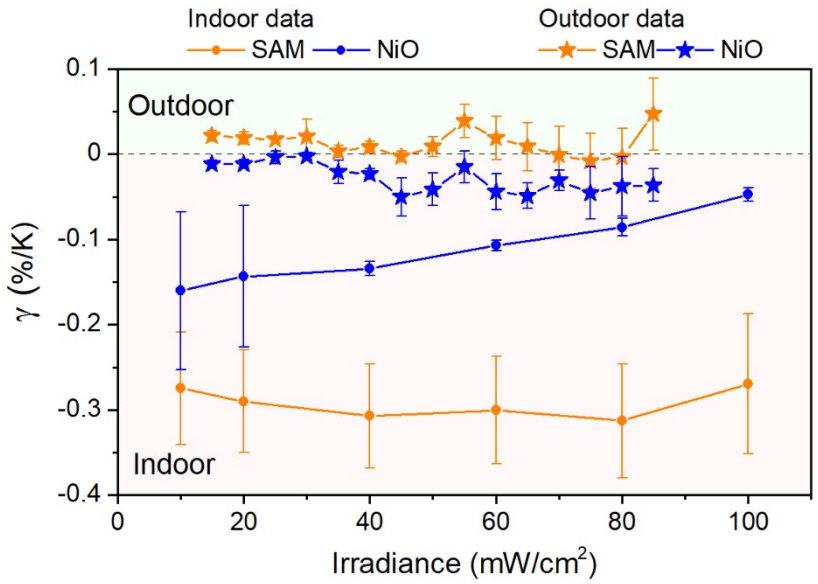

Figure S9 Temperature coefficients for PSCs determined from indoor and short-term (4 days) outdoor measurements. The PSCs here are 3cat_SAM and 3cat_NiO, the data is averaged over 5 cells and error bars represent standard deviation.

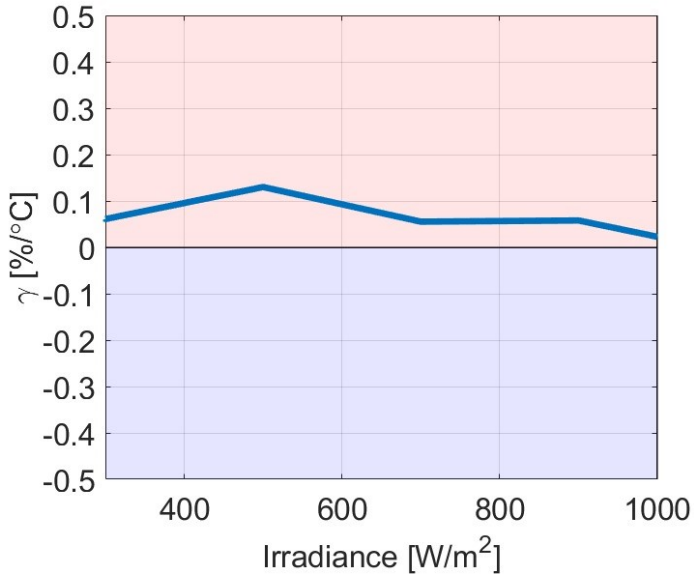

Figure S10 Temperature coefficients for PSCs at different irradiance levels determined from the 11 months-long outdoor data. The PSCs here are 1cat_SAM, using the same dataset as in ***Figure S7.****.*

As discussed in the main text, we believe that the erroneous TCs extracted from the outdoor data may be caused by device meta-stability. In many cases device PCE changes during the day due to light soaking or other effect – *accidentally* – with the same pattern as the cell temperature. Thus, we may observe a positive correlation, which is however not reflecting the device response to change in temperature but overlapping with the transient behaviour on the same timescale. Figure S11 illustrates this idea. Even under indoor conditions of the light cycling experiment the light-soaking improvement can take several hours. Outdoors it will take even longer depending on the irradiance. Such a long improvement in the cell efficiency will coincide in time with the cell temperature which increases during the day due to the irradiance increase. This overlap, in our opinion, may affect the standard procedure of TC extraction from outdoor data.

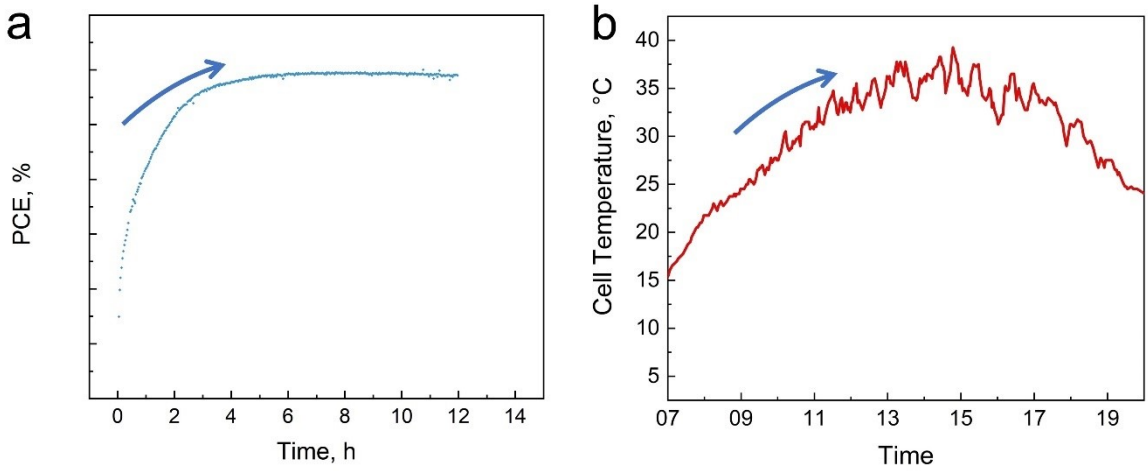

Figure S11 (a) Schematics of changes in 1cat_SAM cell during one cycle of the indoor cycled light experiment. Temperature and other parameters are constant during this experiment and the shape represents dynamic/reversible changes in the device itself. (b) Typical pattern of cell temperature in outdoors exposed samples for one day.

Supplementary Note 5 *Figures of merit for outdoor stability*

There is no universally accepted single metric to track outdoor stability, thus we compared three approaches here (see Figure S12). For indoor ageing, PCE is usually used, however it varies in the outdoor experiments depending on the weather conditions and, - for PSCs, - on the time of day. Therefore, the choice of the time when PCE is recorded and the weather during that time might affect the result [21].

The performance ratio (PR) is used as the main metric for outdoor stability in this study. It was calculated using the following Equation S4:

$$performance\ ratio = \frac{\int_{t_1}^{t_2} P_{mpp}\, dt}{PCE \cdot \int_{t_1}^{t_2} irradiance\, dt}.$$

Equation S4

Here, the power density output (P_{mpp}) is integrated over a given time interval and divided by the integrated irradiance multiplied with the initial PCE measured at standard test conditions.[22] The time interval is set to one day. We then normalised the PR to the energy output of the first full day of exposure. This metric allows monitoring device performance taking into account the transient changes during the diurnal cycle (regardless of the irradiance level on a certain day and the type of the transients of a particular device) [21].

We also used average PCE midday value, averaged between 11:00 and 13:00. By choosing only the period close to midday we limit the impact of transient processes. Power output at a particular light intensity is another possible metric. For demonstration we chose the value of 500 W/m^2 (0.5 Suns) to have multiple occurrences in the wintertime.

In general, the 3 compared figures of merit show similar trends of changes over the year of observations (Figure S12) with a pronounced increase in summer as discussed in the main text. However, the difference between the relative increase in PR and the power at 500 W/m^2 in summer reaches 10-15%, which is noticeable. The procedures for the outdoor stability reporting should be therefore further defined.

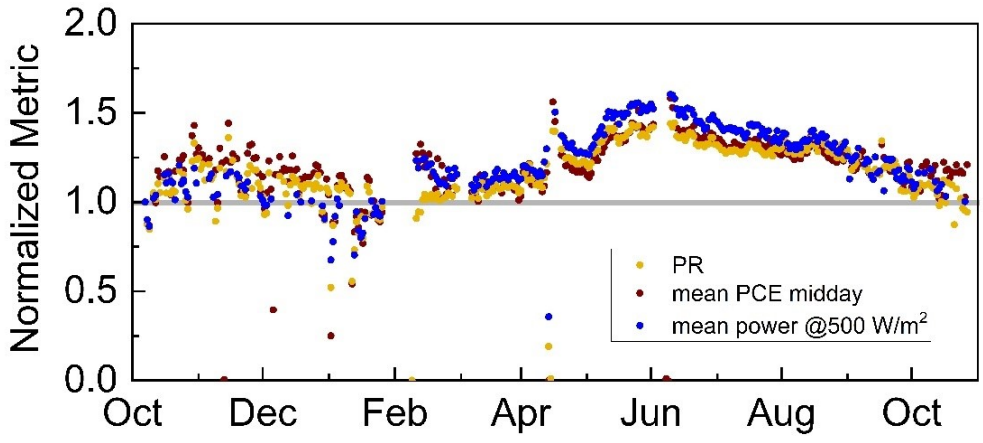

Figure S12 The comparison of different metrices for outdoor stability of (2cat_SAM) PSCs encapsulated through vacuum lamination. All metrices are normalized to the first full day of exposure.

Supplementary Note 6 Statistics and batch-to-batch variations

All the experiments shown in the main section were repeated for several solar cells with the same structure, as detailed in Table S2.

Table S2 Number of cells of each kind studied in each of the ageing scenarios.

Type of the cell	Aging Test		
	Constant light	**Cycled light**	**Outdoor**
1cat_SAM	11 (non encaps) + 6 (encaps)	8	6 (encaps)
2cat_SAM	4 (batch 1) + 4 (batch 2) + 6 (encaps)	5 (batch 1) + 4 (batch 2)	3 (encaps)
3cat_SAM	9	10	9 (encaps)
3cat_NiO	9	12	8 (encaps) + 9 (encaps)

Figure S13 and Figure S14 show the individual MPP tracks recorded for each type of devices in constant and cycled illumination experiments accordingly without averaging. One can see that the particular values and slopes vary slightly while the trends being fairly similar for the majority of the studied cells, except for double cation cells, as discussed below. Average traces, discussed in the main text are therefore justified as representative behaviour of a particular device stack.

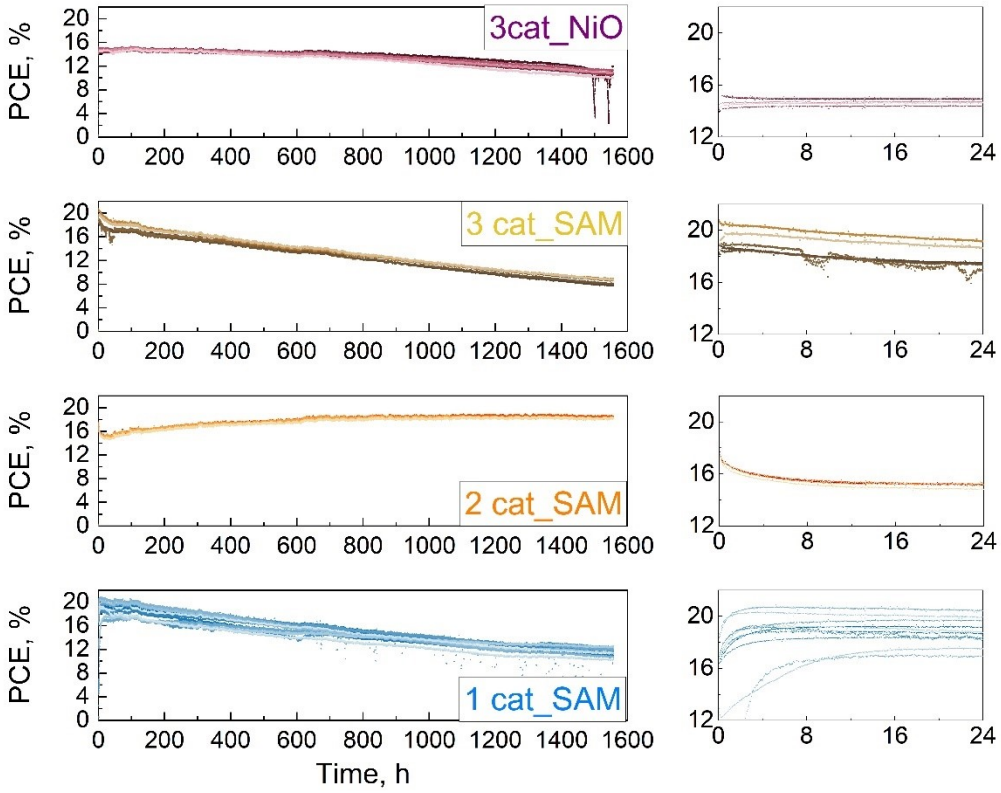

Figure S13 Indoor photo-stability experiment with constant illumination (1 Sun; N2 atmosphere; 25 °C) on 4 types of devices. Each color represents an individual solar cell without averaging. The right column zooms in to the first 24 h of exposure.

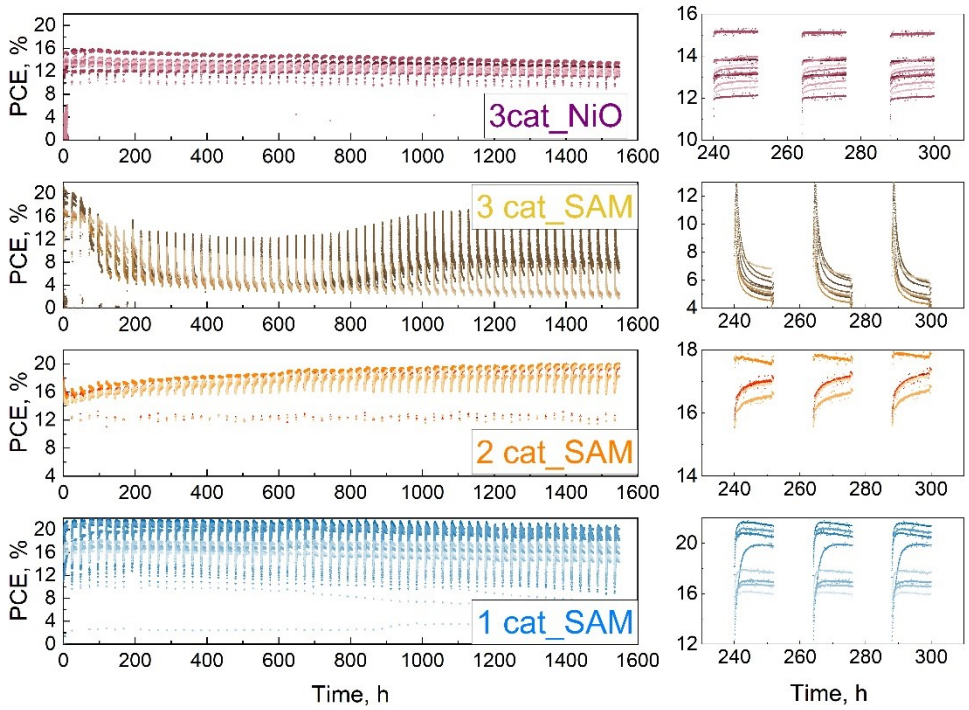

Figure S14 Indoor photo-stability experiment with cycled illumination (1 Sun; N2 atmosphere; 25 °C) on 4 types of devices. Each color represents an individual solar cell without averaging. The right column zooms in to three consecutive cycles.

For double cation PSCs (2cat_SAM) we observed significant batch to batch variation with 2 distinctly different patterns of ageing behaviour. Figure S15 shows the ageing behaviour of all the cells of this type in constant and cycled light experiments. All the cells show initial increase in the device performance, however the batch with higher average initial PCE values changes to a decreasing trend quickly. This decrease is dramatically enhanced with light cycling, making the dynamics similar to 3cat_SAM cells as discussed in the main text or in Figure S14. Only one of these two patterns is shown in the main text to avoid confusions. This pattern is similar to the batch we have outdoors. For the other studied cells, the patters were mostly uniform cell-to-cell and batch-to-batch.

For the cells with simple “glue-based” encapsulation, the outdoor experiments were short term (2-3 weeks) and were repeated twice within the same season. Figure S16 shows the comparison of the two runs. Although temperature and irradiance conditions were somewhat different, the results are in a good qualitative agreement with each other.

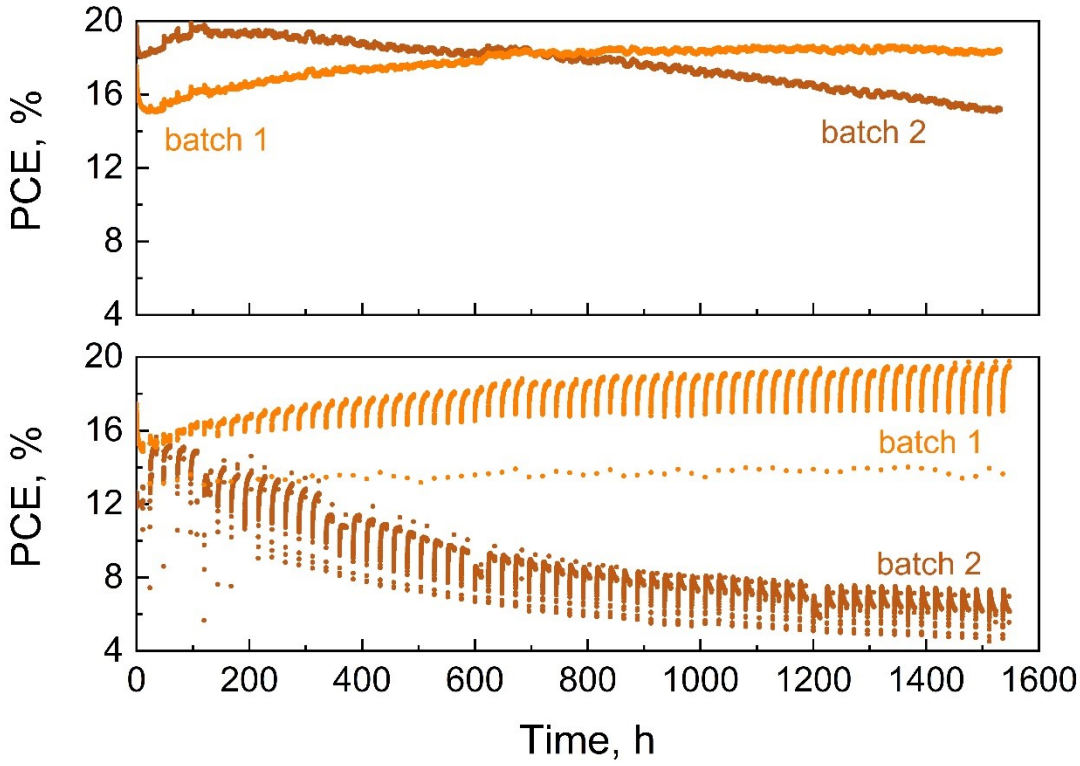

Figure S15 Indoor photo-stability experiments with constant (top) and cycled light (bottom) illumination (1 Sun; N2 atmosphere; 25 °C) on 2cat_SAM cells with high batch-to-batch variations. Each curve represents average results over 4-5 cells from the same batch.

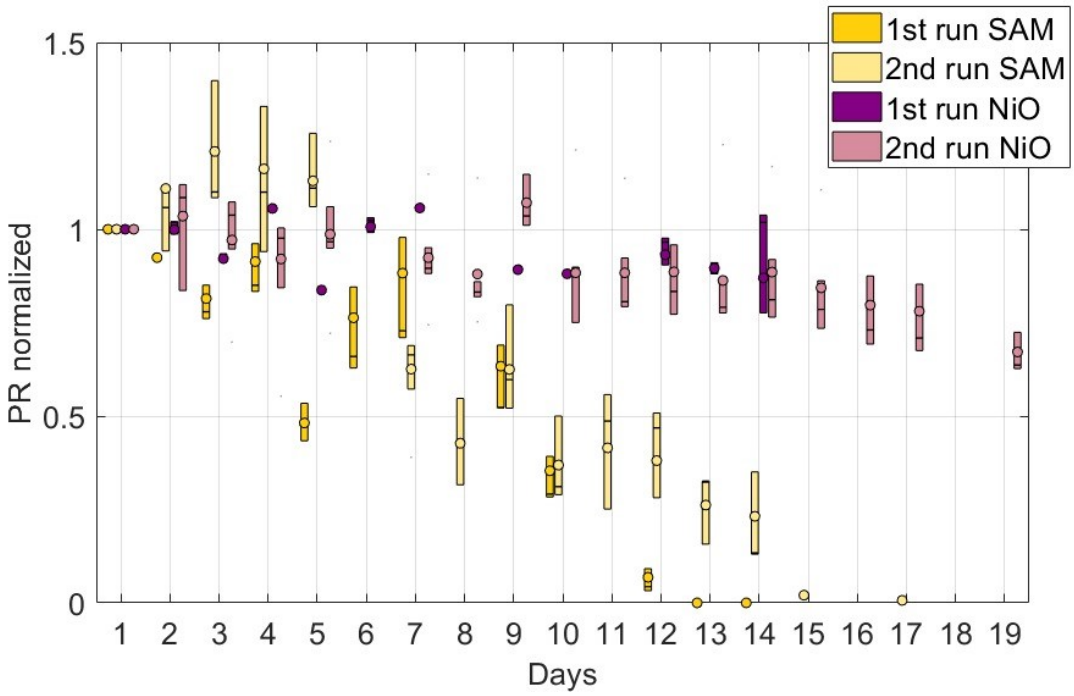

Figure S16 Quartile plot of normalized PR values of two outdoor tests on the triple cation cells with simple glue-based encapsulation. Lines are for the median and circles are for mean values. First run: Averaged over 3 cells for each HTL. Second run: Averaged over 6 cells for SAM and 5 for NiO.

Supplementary Note 7 PCE changes within single cycle in LC experiments

As detailed in Figure S14, the PCE changes within one cycle depend on the PSC architecture. Recovery during the dark phase of the cycle significantly "resets" it, so that the shapes of the neighbouring cycles are very close. However, over longer ageing time the changes accumulate resulting in a significant variation in the cycles' shape. Figure S17 illustrates such changes on the examples of 1cat_SAM and 2cat_SAM cells. The latter upon ageing develops a long light-soaking effect at the beginning of each cycle, which becomes a prevalent reversible process towards the end of the experiment. For 1cat_SAM cells, both increasing and decreasing trends are observed within a cycle. For fresh devices the former process is dominant, however, over time the process responsible for the decreasing behaviour increases in magnitude which changes the overall cycle shape. This represents a characteristic degradation process which can be missed if an inappropriate figure of merit is chosen (such as peak PCE in the cycle for example).

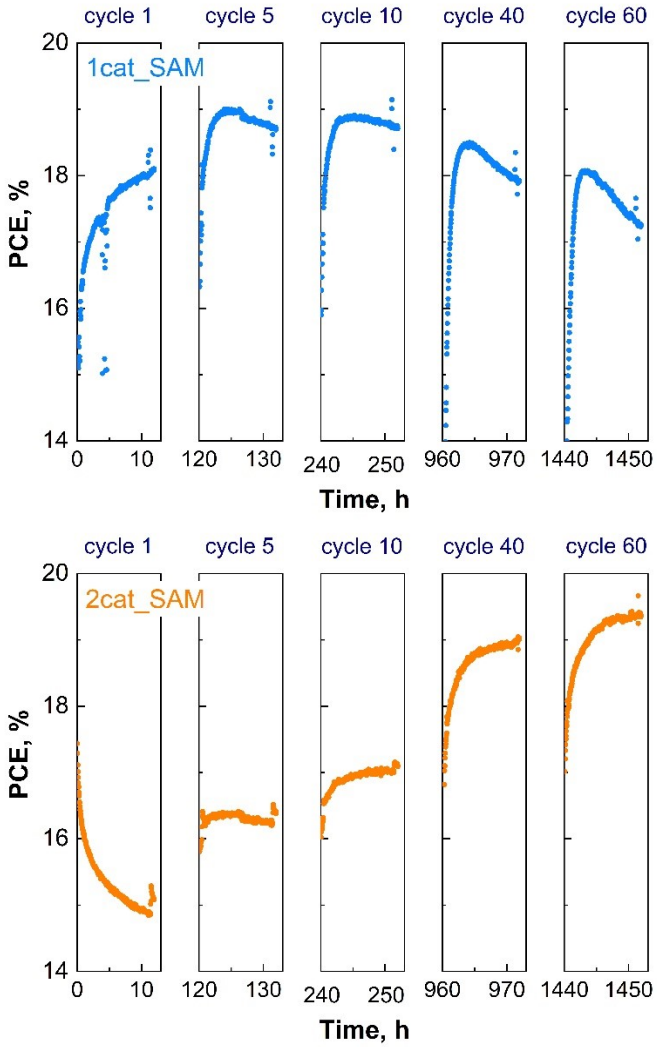

Figure S17 The change in PCE over a single cycle for 1cat_SAM PSCs during the cycled light indoor experiment shown in Figure 1a and 1b.

Supplementary Note 8 Performance ratio in the indoor experiments

For easier comparability of the indoor experiments, the concept of performance ratio can also be used here, like the outdoor one. Using Equation S4 and assuming the constant irradiance level when the light is on, PR can be calculated for the cycled or constant light experiments using 24 h integration periods. In Figure S18 below, the experiments shown in Figure 1 of the main text are summarized as PR evolution over time. It can be seen that 1cat_SAM cells show better stability under cycled light due to dark time recovery, while the opposite is true for the 3cat_SAM devices. 2cat_SAM and 3cat_NiO show comparable stability in both experiments.

When looking at PCE evolution (like in Figure 1 of the main text), it is easy to follow the trend of the peak PCE in each cycle, while changes in the shape of each cycle with aging are easy to miss (see Supplementary Note 7). PR however accounts for the meta-stability and can therefore present a fairer comparison from the position of energy generation. It was previously argued that this is a rational way of comparing cells with different types of transient processes [21].

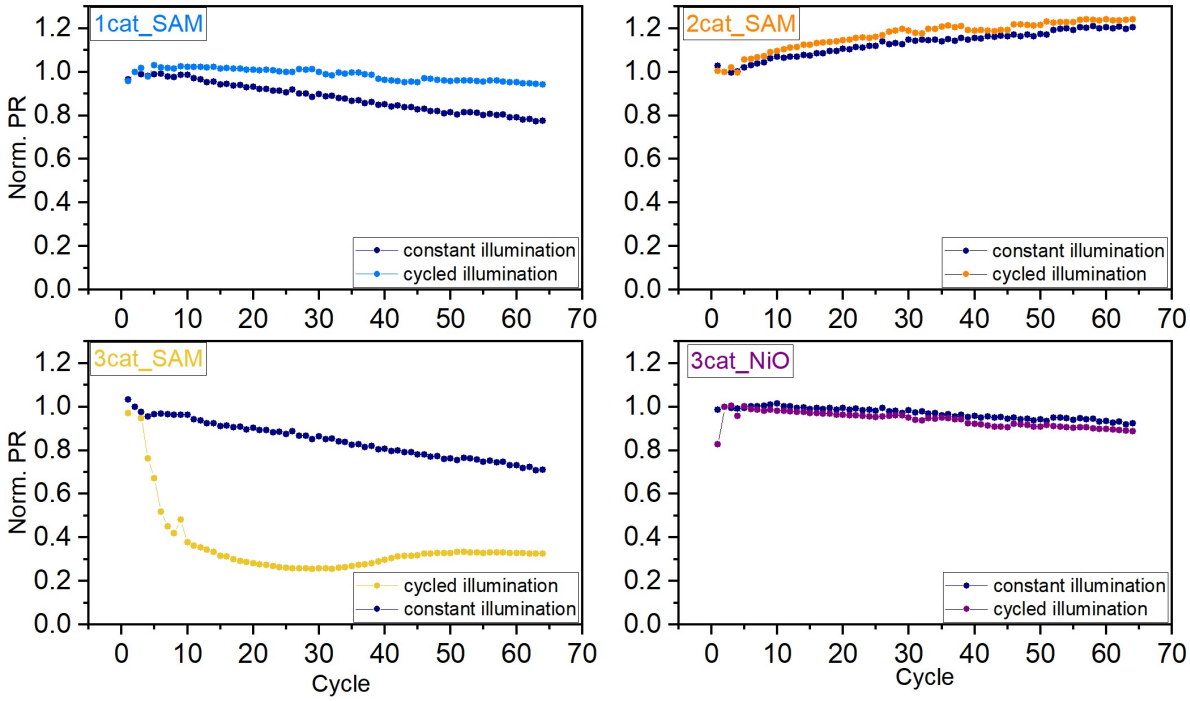

Figure S18 Performance ratio (PR) evolution over time in the indoor experiment with cycled and constant light for 4 types of PSCs. The data are from the same experiment that is shown in Figure 1 in the main text. The data is normalized to the second cycle of exposure.

Supplementary Note 9 Outdoor stability curves in case of moisture penetration

PSCs are known to quickly degrade in presence of humidity. This is due to rapid perovskite decomposition as a result of reaction with water [23]. Therefore, in the event of encapsulation failure during outdoor experiments, the cells quickly change the colour from the dark brown to yellow accompanied by rapid drop in the device PCE. This was the case for some experiments using glue-based encapsulation, particularly (3cat_SAM) shown in Figure 2 in the main text (see photos in Figure S19).

Moisture penetration through the barrier layers is a diffusion limited process, and as such was previously suggested to be fitted with an error function [24]. Here we show that such fitting might be suitable for PSCs in our case. As explained in Figure S20 initial part of the curve (before encapsulation failure) is fitted using the fit curve from the indoor cycled light experiment, that is then multiplied by the error function to represent moisture ingress process. We can therefore conclude that the initial decay in the outdoor data is not related to the encapsulation issues, but to the photo-stability of the cell itself.

We would also like to note, that all other cells in this work that were exposed outdoors are encapsulated using vacuum lamination and showed no visible colour changes during the entire duration of outdoor experiments.

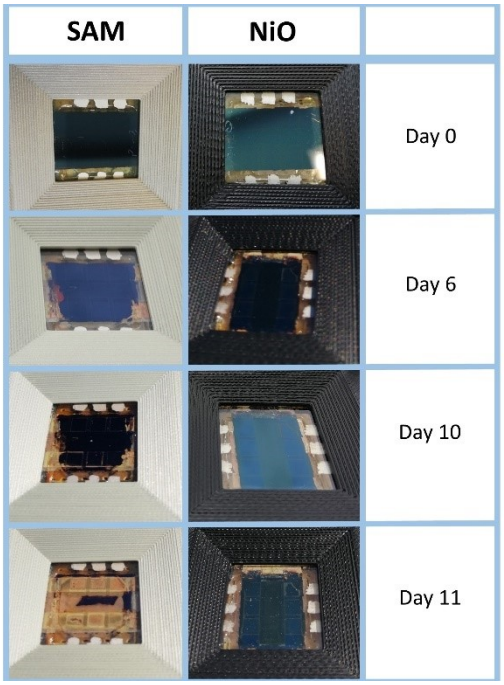

Figure S19 Images of the triple cation PSCs with different transport layers (3cat_SAM and 3cat_NiO) with a simple glue-based encapsulation after certain time outdoors. Both were encapsulated with a simple glue-based procedure. Clear discoloration of 3cat_SAM cells is due to perovskite decomposition in presence of humidity, indicating failure of encapsulation.

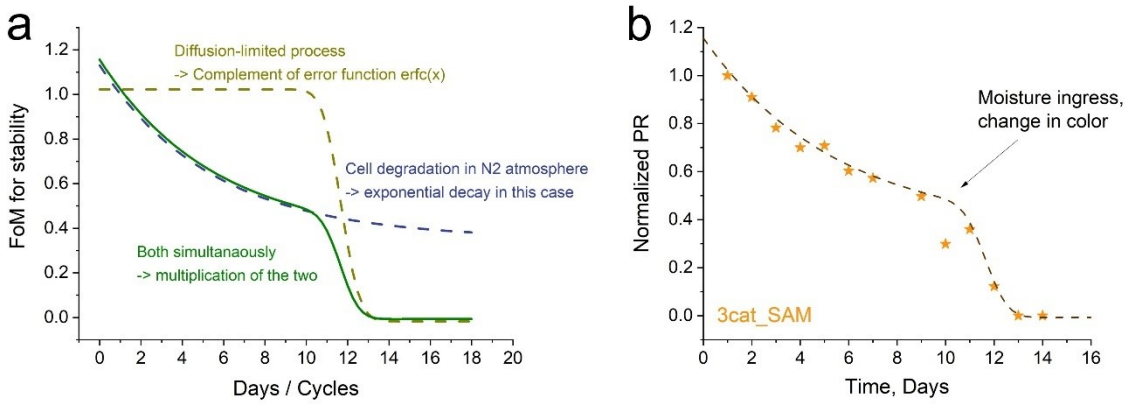

Figure S20 The fit for the outdoor degradation curve for 3cat_SAM PSCs. (a) Schematic explanation of the fitting curve which is a superposition of two functions: one representing the initial degradation behavior in the indoor LC experiment (Figure 1c in the main text), and the other – the breakdown of encapsulation (we used error function for this diffusion limited process). Figure (b) shows this fit with the outdoor data on cells that experienced perovskite decomposition.

Supplementary Note 10 Impact of encapsulation on the PSCs photo-stability

Indoor tests in this work are conducted in nitrogen atmosphere, therefore the samples require no encapsulation to protect them from the impact of oxygen and humidity. However, encapsulation using a vacuum lamination process was previously reported in literature to also increase perovskite photo-stability in some perovskite cells [25]. The mechanism behind such improvement is the trapping of perovskite decomposition products within the encapsulation with their subsequent conversion back to perovskite. To check if encapsulation affected the photo-stability in our cells, we conducted a test to verify the effect.
Figure S21 compares the PSCs with and without encapsulation under nitrogen atmosphere in a constant illumination experiment (1sun, MPP tracking, ~30 °C). As seen from the figure, encapsulation does not improve the stability of studied cells and the ageing trends are similar regardless of encapsulation. We, therefore, conclude that comparison between outdoor and indoor ageing experiments shown in the manuscript is valid even though cells were encapsulated for the outdoor studies but not for indoor ones, performed under inert conditions.

While the general decreasing trend is observed for both encapsulated and not encapsulated devices in the case of 1cat_SAM cells, there is a noticeable increase in degradation rate for encapsulated devices. Such effect might be caused by slightly higher temperature (about 5 °C) for the encapsulated devices, where the encapsulation hinders direct connection to the cooling system. Further studies on the effects of encapsulation on photo-stability for different PSC architectures are certainly required.

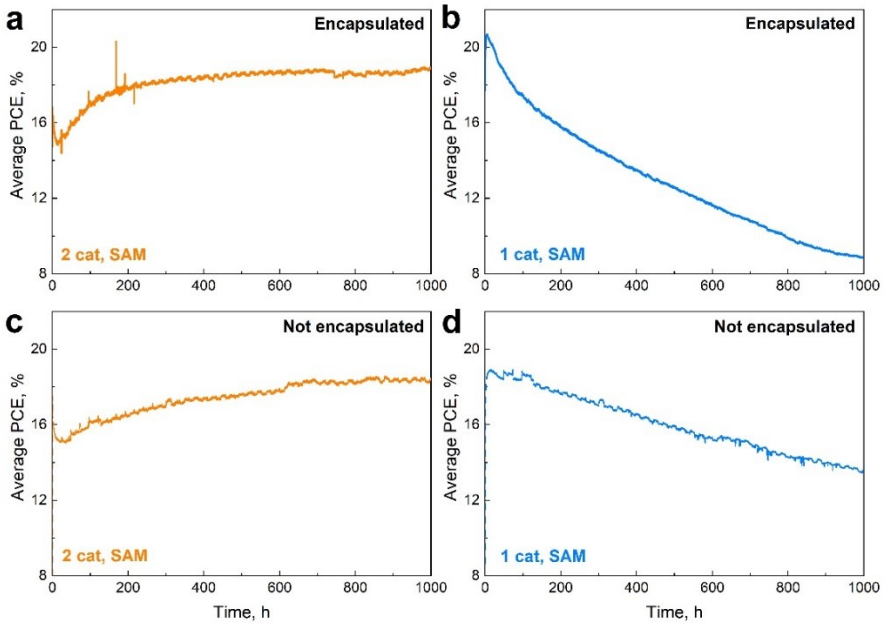

Figure S21 Indoor photo-stability experiment with MPP tracking under constant light illumination for 2cat_SAM (a,c) and 1cat_SAM (b,d) PSCs with (a,b) or without (c,d) encapsulation. The encapsulation is made with vacuum lamination the same as for the cells exposed outdoor. Each curve is an average over 4 to 11 devices.

Supplementary Note 11 Indoor and outdoor PCE measurements for PSCs exposed outdoors

In the long-term outdoor experiment shown in Figure 4 of the main text, the performance ratio did not show significant degradation if compared, e.g., summer-to-summer. The same is true if one considers instantaneous power output or PCE values measured outdoors (see Figure S22). However, the indoor measurement at STC conditions conducted after ~2 years of exposure showed ~20% lower efficiency compared to the initial value. One might conclude that the device lost efficiency during the outdoor exposure. Yet, these indoor measurements were conducted with only 10-15 minutes of light soaking. As can be seen from Figure S16, for 2cat_SAM cells, aging causes an increase in the light-soaking duration required to reach the peak PCE; resulting time-to-peak are in the range of dozens of hours rather than minutes. Therefore, the apparent contradiction between indoor and outdoor PCE results may originate from the complex dynamic effects in aged cells that are not appreciated by the relatively quick JV measurements without extensive preconditioning. Due to technical reasons, it was not possible to perform more frequent another indoor JV measurements on this batch without risking damaging the cells irreversibly, hindering to confirm this. We believe some of the effects are not saturated within a single day-night cycle either and the cell history plays a critical role. As another example of the pronounced impact of the measurement's history, we noticed that outdoor-aged 2cat_SAM cells show a pronounced decrease in PCE when stored in the dark

for several days if compared to the performance after one night of storage as in real-world conditions. This decrease can also be reversed after several hours of light soaking.

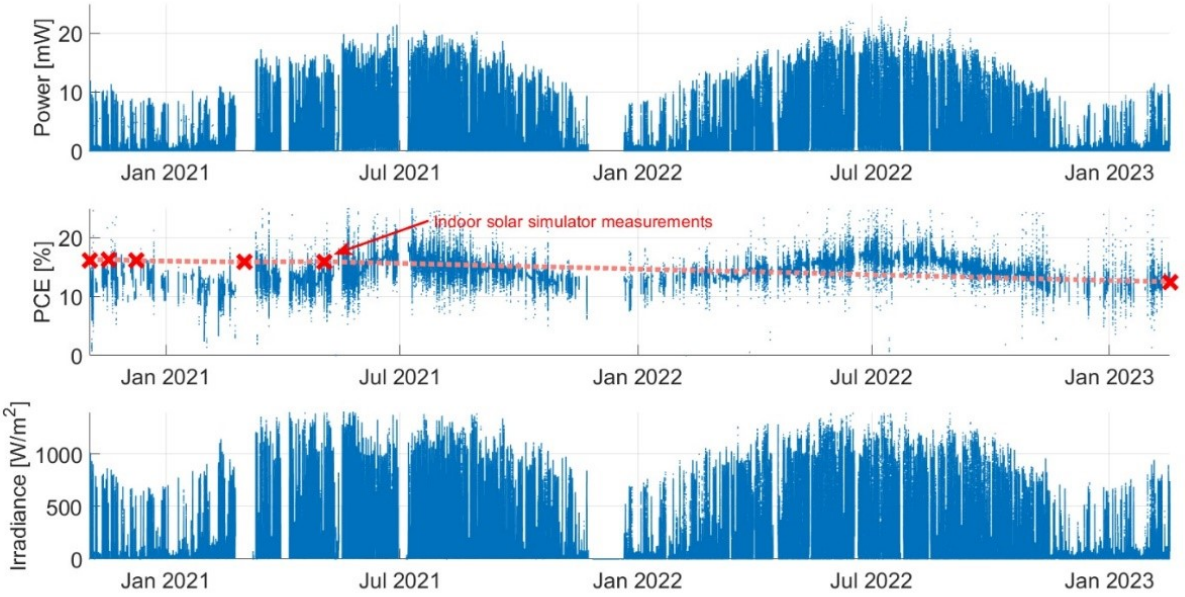

Figure S22 Long-term outdoor data of the oldest encapsulated 2cat_SAM PSC on our test field. The top panel shows the cell power output, the bottom panel show the irradiance in the plane of array recorded outdoor. The PCE values in the middle panel are only shown in the midday (between 11:00 and 15:00) and only under irradiance >200 W/m2; red crossed in the panel mark the PCE of the cell measured indoors under sun simulator after 10-15 minutes of light soaking.

Supplementary Note 12 Impact of meta-stability on seasonal changes in VMPP during a year

To explain unusual seasonal changes observed in our PSCs, we analysed the evolution of devices V_{MPP} over a year in PSC (encapsulated with "3 glass encapsulation") with different extent of meta-stability as well as in a silicon solar cell (see Figure S23). In the silicon solar cell, we observe a slight decrease in voltage during the summer period due to the higher temperatures. In contrast, PSCs show a decrease in voltage during the winter, that is going back close to the original value towards next summer. As discussed in Supplementary Note 4, this does not reflect positive temperature coefficients, but rather highlights pronounced meta-stability in perovskite-based cells. 3cat_NiO cells that show only marginal magnitude of reversible changes (see Figure S14) also show a marginal winter drop in V_{MPP}, instead, it slowly irreversible degrades somewhat similar to the indoor tests shown in Figure 1. However, the devices with large extent of meta-stability show a very pronounced seasonal fluctuation during outdoor exposures. These changes are the result of the incomplete light soaking during the low irradiance and low temperature

part of the year. It is further exaggerated as the extent of light-soaking changes is increased with an increase of the dark storage time, thus having a "memory" effect exceeding a single day-night cycle. We noticed that the cells exposed outdoors, show significantly lower V_{OC} and require significantly longer light-soaking times to recover if they were stored in the dark before the measurement. 2cat_SAM (not shown in Figure S23) devices with a similar large seasonal response shown in Figure 4 have qualitatively similar behaviour to 1cat_SAM with significant decrease in V_{MPP} in winter.

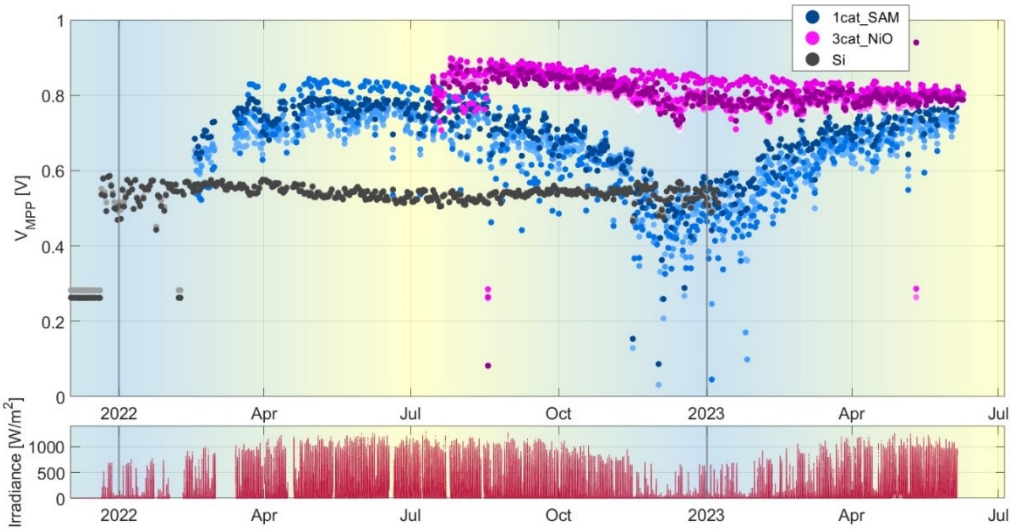

Figure S23 The evolution of V_{MPP} during one year of outdoor exposure of 1cat_SAM (high magnitude of meta-stability), 3cat_NiO (low magnitude of meta-stability) and small-area silicon solar cell. The datapoints represent median values per day between 10:00 and 17:59, without further filtering. Filtering for certain irradiance levels does not affect the trends. The bottom panel shows irradiance during the outdoor experiment.

References

1 A. Al-Ashouri, A. Magomedov, M. Roß, M. Jošt, M. Talaikis, G. Chistiakova, T. Bertram, J. A. Márquez, E. Köhnen, E. Kasparavičius, S. Levcenco, L. Gil-Escrig, C. J. Hages, R. Schlatmann, B. Rech, T. Malinauskas, T. Unold, C. A. Kaufmann, L. Korte, G. Niaura, V. Getautis and S. Albrecht, *Energy Environ. Sci.*, 2019, **12**, 3356–3369.

2 D. Di Girolamo, F. Matteocci, F. U. Kosasih, G. Chistiakova, W. Zuo, G. Divitini, L. Korte, C. Ducati, A. Di Carlo, D. Dini and A. Abate, *Advanced Energy Materials*, 2019, **9**, 1901642.

3 J. Li, J. Dagar, O. Shargaieva, O. Maus, M. Remec, Q. Emery, M. Khenkin, C. Ulbrich, F. Akhundova, J. A. Márquez, T. Unold, M. Fenske, C. Schultz, B. Stegemann, A. Al-Ashouri, S. Albrecht, H. Koebler, A. Abate, D. Toebbens, I. Zizak, E. List-Kratochvil and E. Unger, 2021.

4 M. Saliba, T. Matsui, J.-Y. Seo, K. Domanski, J.-P. Correa-Baena, M. K. Nazeeruddin, S. M. Zakeeruddin, W. Tress, A. Abate, A. Hagfeldt and M. Grätzel, *Energy Environ. Sci.*, 2016, **9**, 1989–1997.
5 A. Magomedov, A. Al-Ashouri, E. Kasparavičius, S. Strazdaite, G. Niaura, M. Jošt, T. Malinauskas, S. Albrecht and V. Getautis, *Advanced Energy Materials*, 2018, **8**, 1801892.
6 Q. Emery, M. Remec, G. Paramasivam, S. Janke, J. Dagar, C. Ulbrich, R. Schlatmann, B. Stannowski, E. Unger and M. Khenkin, *ACS Appl. Mater. Interfaces*, 2022, **14**, 5159–5167.
7 M. V Khenkin, E. A. Katz, A. Abate, G. Bardizza, J. J. Berry, C. Brabec, F. Brunetti, V. Bulović, Q. Burlingame, A. Di Carlo, R. Cheacharoen, Y. B. Cheng, A. Colsmann, S. Cros, K. Domanski, M. Dusza, C. J. Fell, S. R. Forrest, Y. Galagan, D. Di Girolamo, M. Grätzel, A. Hagfeldt, E. von Hauff, H. Hoppe, J. Kettle, H. Köbler, M. S. Leite, S. (Frank) Liu, Y. L. Loo, J. M. Luther, C. Q. Ma, M. Madsen, M. Manceau, M. Matheron, M. McGehee, R. Meitzner, M. K. Nazeeruddin, A. F. Nogueira, Ç. Odabaşı, A. Osherov, N. G. Park, M. O. Reese, F. De Rossi, M. Saliba, U. S. Schubert, H. J. Snaith, S. D. Stranks, W. Tress, P. A. Troshin, V. Turkovic, S. Veenstra, I. Visoly-Fisher, A. Walsh, T. Watson, H. Xie, R. Yıldırım, S. M. Zakeeruddin, K. Zhu and M. Lira-Cantu, *Nature Energy*, 2020, **5**, 35–49.
8 T. J. Jacobsson, A. Hultqvist, A. García-Fernández, A. Anand, A. Al-Ashouri, A. Hagfeldt, A. Crovetto, A. Abate, A. G. Ricciardulli, A. Vijayan, A. Kulkarni, A. Y. Anderson, B. P. Darwich, B. Yang, B. L. Coles, C. A. R. Perini, C. Rehermann, D. Ramirez, D. Fairen-Jimenez, D. Di Girolamo, D. Jia, E. Avila, E. J. Juarez-Perez, F. Baumann, F. Mathies, G. S. A. González, G. Boschloo, G. Nasti, G. Paramasivam, G. Martínez-Denegri, H. Näsström, H. Michaels, H. Köbler, H. Wu, I. Benesperi, M. I. Dar, I. Bayrak Pehlivan, I. E. Gould, J. N. Vagott, J. Dagar, J. Kettle, J. Yang, J. Li, J. A. Smith, J. Pascual, J. J. Jerónimo-Rendón, J. F. Montoya, J.-P. Correa-Baena, J. Qiu, J. Wang, K. Sveinbjörnsson, K. Hirselandt, K. Dey, K. Frohna, L. Mathies, L. A. Castriotta, M. H. Aldamasy, M. Vasquez-Montoya, M. A. Ruiz-Preciado, M. A. Flatken, M. V. Khenkin, M. Grischek, M. Kedia, M. Saliba, M. Anaya, M. Veldhoen, N. Arora, O. Shargaieva, O. Maus, O. S. Game, O. Yudilevich, P. Fassl, Q. Zhou, R. Betancur, R. Munir, R. Patidar, S. D. Stranks, S. Alam, S. Kar, T. Unold, T. Abzieher, T. Edvinsson, T. W. David, U. W. Paetzold, W. Zia, W. Fu, W. Zuo, V. R. F. Schröder, W. Tress, X. Zhang, Y.-H. Chiang, Z. Iqbal, Z. Xie and E. Unger, *Nat Energy*, 2022, **7**, 107–115.
9 H. Köbler, S. Neubert, M. Jankovec, B. Glažar, M. Haase, C. Hilbert, M. Topič, B. Rech and A. Abate, *Energy Technology*, 2022, **10**, 2200234.
10 L. Rakocevic, F. Ernst, N. T. Yimga, S. Vashishtha, T. Aernouts, T. Heumueller, C. J. Brabec, R. Gehlhaar and J. Poortmans, *Solar RRL*, 2019, **3**, 1800287.
11 A. Al-Ashouri, E. Köhnen, B. Li, A. Magomedov, H. Hempel, P. Caprioglio, J. A. Márquez, A. B. Morales Vilches, E. Kasparavicius, J. A. Smith, N. Phung, D. Menzel, M. Grischek, L. Kegelmann, D. Skroblin, C. Gollwitzer, T. Malinauskas, M. Jošt, G. Matič, B. Rech, R. Schlatmann, M. Topič, L. Korte, A. Abate, B. Stannowski, D. Neher, M. Stolterfoht, T. Unold, V. Getautis and S. Albrecht, *Science*, 2020, **370**, 1300–1309.
12 M. Jošt, B. Lipovšek, B. Glažar, A. Al-Ashouri, K. Brecl, G. Matič, A. Magomedov, V. Getautis, M. Topič and S. Albrecht, *Advanced Energy Materials*, 2020, **10**, 2000454.
13 C. N. Jardine, T. Betts, R. Gottschalg, D. Infield and K. Lane, Conference: Proceedings Photovoltaic in Europe Conference, 2002.
14 P. Rodrigo, E. Fernández, F. Almonacid and P. Pérez-Higueras, 2017, **163**, 73–90.
15 E. Velilla, F. Jaramillo and I. Mora-Seró, *Nat Energy*, 2021, **6**, 54–62.
16 V. Stoichkov, N. Bristow, J. Troughton, F. De Rossi, T. M. Watson and J. Kettle, *Solar Energy*, 2018, **170**, 549–556.
17 T. Moot, J. B. Patel, G. McAndrews, E. J. Wolf, D. Morales, I. E. Gould, B. A. Rosales, C. C. Boyd, L. M. Wheeler, P. A. Parilla, S. W. Johnston, L. T. Schelhas, M. D. McGehee and J. M. Luther, *ACS Energy Lett.*, 2021, **6**, 2038–2047.
18 W. Tress, K. Domanski, B. Carlsen, A. Agarwalla, E. A. Alharbi, M. Graetzel and A. Hagfeldt, *Nat Energy*, 2019, **4**, 568–574.

19 A. Manekkathodi, B. Aïssa, A. Belaidi and S. Ashhab, *J. Phys. Chem. C*, 2020, **124**, 9118–9125.
20 T. J. Silverman, M. G. Deceglie, B. Marion, S. Cowley, B. Kayes and S. Kurtz, *Outdoor Performance of a Thin-Film Gallium-Arsenide Photovoltaic Module*, National Renewable Energy Lab. (NREL), Golden, CO (United States), 2013.
21 M. V. Khenkin, A. K. M, I. Visoly-Fisher, Y. Galagan, F. D. Giacomo, B. R. Patil, G. Sherafatipour, V. Turkovic, H.-G. Rubahn, M. Madsen, T. Merckx, G. Uytterhoeven, J. P. A. Bastos, T. Aernouts, F. Brunetti, M. Lira-Cantu and E. A. Katz, *Energy Environ. Sci.*, 2018, **11**, 739–743.
22 IEC 61724-1:2017 | IEC Webstore | rural electrification, solar power, solar panel, photovoltaic, PV, smart city, LVDC, https://webstore.iec.ch/publication/33622, (accessed April 16, 2021).
23 J. Huang, S. Tan, P. D. Lund and H. Zhou, *Energy Environ. Sci.*, 2017, **10**, 2284–2311.
24 R. Roesch, T. Faber, E. von Hauff, T. M. Brown, M. Lira-Cantu and H. Hoppe, *Advanced Energy Materials*, 2015, **5**, 1501407.
25 L. Shi, M. P. Bucknall, T. L. Young, M. Zhang, L. Hu, J. Bing, D. S. Lee, J. Kim, T. Wu, N. Takamure, D. R. McKenzie, S. Huang, M. A. Green and A. W. Y. Ho-Baillie, *Science*, 2020, **368**, eaba2412.